Propagation, breaking and interaction of regular and irregular waves over a complex bathymetry with an oil rig

Zaman, Hasanat; Akinturk, Ayhan; Mak, Lawrence

[Proceedings of OCEANS-2021], 2021-09-30

Propagation, breaking and interaction of regular and irregular waves over a complex bathymetry with an oil rig

Hasanat Zaman
Ocean, Coastal and River
Engineering Research Center
National Research Council Canada
St. John's, NL Canada
Hasanat.Zaman@nrc-cnrc.gc.ca

Ayhan Akinturk
Ocean, Coastal and River
Engineering Research Center
National Research Council Canada
St. John's, NL Canada
Ayhan.Akinturk@nrc-cnrc.gc.ca

Lawrence Mak
Ocean, Coastal and River
Engineering Research Center
National Research Council Canada
St. John's, NL Canada
Lawrence.Mak@nrc-cnrc.gc.ca

***Abstract*— The oil and gas platform in the nearshore and offshore region are sometimes vulnerable due to the extremely high waves approaching the structure. The bathymetry of such a region plays a vibrant role in modifying the incoming wave fields. Depending on the changes of bathymetry, the deepwater wave can change into a shallow water wave and could cause wave shoaling, modification in wavelength, and in many cases leads to wave breaking. After breaking the leftover wave energy is reformed and keeps propagating. A 3D dispersive numerical model is developed and utilized for the prediction of the wave reflection, diffraction, breaking, and propagation in the presence of varying water depth and an offshore oil rig. A finite difference method has been employed for the numerical computation that uses ADI (Alternating Direction Implicit) algorithm. In this work, a sea bottom of varying bathymetry is utilized extended from a deeper region to a shallower region may be treated as a natural or an artificial submerged obstacle or sea bottom. A square shaft of an oil and gas platform is located in the shallower region. In the simulation, a set of relevant regular and irregular waves are studied. Limited field data of irregular waves are used for model validation.**

Keywords—Extreme waves, 3D numerical model, uneven bottom, ocean structure, field data, result comparisons.

I. INTRODUCTION

During the propagation, waves undergo a lot of changes to their physical and dynamic characteristics. When waves approach the shallower region wavelengths are shortened and if there is no breaking then the wave height increases to maintain the conservation of energy. On the other hand, wave breaking takes place when the increase of the wave heights reaches their breaking criteria. In that case, the waves break, lose their energies, and reform to continue their propagation further. Shallow water wave or long period wave is well known for imparting considerable difficulties to different coastal and offshore facilities. In normal or abnormal weather conditions, they are known to be the cause of huge damages to the anchored ships and mooring systems. This kind of wave can cause severe damages to the ocean structures and/or can reduce the workability and performance tremendously. There are different numerical approaches were carried out by different researchers to understand the propagation, modifications, and loadings of such waves on the ocean structures. The use of vertically integrated numerical models is very popular and advantageous for low computation time and accuracy as it has been reported by many researchers that the approximation by the recent vertically integrated models, for example, Boussinesq or other types of models agree well with the relevant physical experiments or field observations. The advantage of such models is that they can be useful to study the wave propagation including breaking (Svendsen et al., 1996) for a wide range of areas from the deep sea to the shallow water (Sørensen et. al., 1996) region with confidence. Essentially ocean wave field contains waves of different heights, frequencies, and directions. The wave field is transformed and it experiences a lot of changes into its basic feature when it moves towards the shallow region from the offshore region due to changes in water depths. Researchers have been extending their effort to fabricate numerical models into the most attractive form. Abbotts et al. (1978), Bayram and Larson (2000), Flaten and Rygg (1991), Sato et al. (1992), Karambas and Koutitas (1992), Madsen and Sørensen (1992), Peregrine (1967), Hiraishi et al (1995), Zaman (2007) are some to mention. In this study, a vertically integrated model is developed and utilized to study the propagation of regular and irregular waves over a natural or man-made elevated bottom followed by an operational oil rig. The basic physics of the present model follows the description of Hiraishi et al (1995). An enhanced dispersion relation has been invoked in the simulation. This study aims to perceive the transformation of incoming waves energies from the offshore area to the vicinity of the oil rig.

II. Numerical Model

The numerical model used here is formulated by vertical integration of the continuity equation and equations of motions. The basic equations are as follows:

$$\frac{\partial \eta}{\partial x}+\frac{\partial}{\partial t}\int_{-h}^{\eta} udz+\frac{\partial}{\partial t}\int_{-h}^{\eta} vdz=0 \tag{1}$$

$$\begin{aligned}
&\frac{\partial}{\partial t}\int_{-h}^{\eta} udz+\frac{\partial}{\partial x}\left[\left(\int_{-h}^{\eta} udz\int_{-h}^{\eta} udz\right)/(h+\eta)\right]\\
&+\frac{\partial}{\partial y}\left[\left(\int_{-h}^{\eta} udz\int_{-h}^{\eta} vdz\right)/(h+\eta)\right]+g(h+\eta)\frac{\partial \eta}{\partial x}\\
&+\kappa\int_{-h}^{\eta} udz+\frac{f_d}{2(h+\eta)^2}\int_{-h}^{\eta} udz\sqrt{\left(\int_{-h}^{\eta} udz\right)^2+\left(\int_{-h}^{\eta} vdz\right)^2}\\
&=\mu\left(\frac{\partial^2}{\partial x^2}\int_{-h}^{\eta} udz+\frac{\partial^2}{\partial y^2}\int_{-h}^{\eta} udz\right)\\
&+\left(A+\frac{1}{3}\right)h^2\left(\frac{\partial^3}{\partial x^2\partial t}\int_{-h}^{\eta} udz+\frac{\partial^3}{\partial x\partial y\partial t}\int_{-h}^{\eta} vdz\right)\\
&+Agh^3\left(\frac{\partial^3\eta}{\partial x^3}+\frac{\partial \eta}{\partial x\partial y^2}\right)\\
&+h\frac{\partial h}{\partial x}\left(\frac{1}{3}\frac{\partial^2}{\partial x\partial t}\int_{-h}^{\eta} udz+\frac{1}{6}\frac{\partial^2}{\partial y\partial t}\int_{-h}^{\eta} vdz\right)\\
&+h\frac{\partial h}{\partial y}\left(\frac{1}{6}\frac{\partial^2}{\partial y\partial t}\int_{-h}^{\eta} vdz\right)\\
&+Agh^2\left[\frac{\partial h}{\partial x}\left(2\frac{\partial^2\eta}{\partial x^2}+\frac{\partial^2\eta}{\partial y^2}\right)+\frac{\partial h}{\partial y}\frac{\partial^2\eta}{\partial x\partial y}\right]
\end{aligned} \tag{2}$$

$$\begin{aligned}
&\frac{\partial}{\partial t}\int_{-h}^{\eta} vdz+\frac{\partial}{\partial x}\left[\left(\int_{-h}^{\eta} udz\int_{-h}^{\eta} vdz\right)/(h+\eta)\right]\\
&+\frac{\partial}{\partial y}\left[\left(\int_{-h}^{\eta} vdz\int_{-h}^{\eta} vdz\right)/(h+\eta)\right]+g(h+\eta)\frac{\partial \eta}{\partial y}\\
&+\kappa\int_{-h}^{\eta} vdz+\frac{f_d}{2(h+\eta)^2}\int_{-h}^{\eta} vdz\sqrt{\left(\int_{-h}^{\eta} udz\right)^2+\left(\int_{-h}^{\eta} vdz\right)^2}\\
&=\mu\left(\frac{\partial^2}{\partial x^2}\int_{-h}^{\eta} udz+\frac{\partial^2}{\partial y^2}\int_{-h}^{\eta} vdz\right)\\
&+\left(A+\frac{1}{3}\right)h^2\left(\frac{\partial^3}{\partial y^2\partial t}\int_{-h}^{\eta} vdz+\frac{\partial^3}{\partial x\partial y\partial t}\int_{-h}^{\eta} udz\right)\\
&+Agh^3\left(\frac{\partial^3\eta}{\partial y^3}+\frac{\partial \eta}{\partial x^2\partial y}\right)\\
&+h\frac{\partial h}{\partial y}\left(\frac{1}{3}\frac{\partial^2}{\partial y\partial t}\int_{-h}^{\eta} vdz+\frac{1}{6}\frac{\partial^2}{\partial x\partial t}\int_{-h}^{\eta} udz\right)\\
&+h\frac{\partial h}{\partial x}\left(\frac{1}{6}\frac{\partial^2}{\partial y\partial t}\int_{-h}^{\eta} vdz\right)\\
&+Agh^2\left[\frac{\partial h}{\partial y}\left(2\frac{\partial^2\eta}{\partial y^2}+\frac{\partial^2\eta}{\partial x^2}\right)+\frac{\partial h}{\partial x}\frac{\partial^2\eta}{\partial x\partial y}\right]
\end{aligned} \tag{3}$$

where η is the free surface at any given time, t the time, u and v the velocities in the x and y directions, $\int_{-h}^{\eta} udz$ the mass flux in the x-direction, $\int_{-h}^{\eta} vdz$ the mass flux in the y-direction, g the gravitational acceleration, h the still water depth at any location, $h+\eta$ the instantaneous water depth at any location in the domain, κ the boundary dumping function varies linearly along the width of the wave absorbing layers and null elsewhere, μ the eddy viscosity defines the momentum exchange due to turbulence and f_d is the energy dissipation coefficient used for the energy damping expression. A wave absorbing layer is a numerical energy-dumping zone in the model. It is usually utilized around the outer boundary of the computational domain to reduce or eliminate reflected wave components from the domain boundaries or behaves like an open boundary. Width with twice the incident wavelength provides an effective absorbing efficiency. The parameter A is an important factor incorporated through the dispersion relation to improving the computational error in the wave celerity and group velocity. See Madsen and Sørensen (1992) for details.

For the better prediction of the wavenumber, the following dispersion relation is utilized in the numerical simulation:

$$c=\sqrt{g\frac{A+k^{-2}h^{-1}}{(A+1/3)+k^{-2}h^{-2}}} \tag{4}$$

as per the frequency dispersion obtained from Padé's (2,2) expansion of Stoke's first-order theory, the parameter A becomes 1/15, k is the wavenumber and c is the wave celerity. The expression (Bayram and Larson, 2000) for eddy viscosity can be defined for this model as follows:

$$\mu=\sqrt{\frac{\alpha^2 d g^3 s(\widehat{M}-M_r)}{\sigma^4(M_s-M_r)}} \tag{5}$$

where α(=2.5) is a coefficient valid in the surf zone type region and λ the angle of the bottom slope, d the mean water depth, σ the angular frequency, $\widehat{M}$ the flow amplitude, M_s the wave-induced flow, $s=tan\lambda$ is the bottom slope and M_r is the reformed wave amplitude.

$$M_s=(0.228+2.12s)\ g^{1/2}d^{3/2} \tag{6}$$

$$M_r=0.135\ g^{1/2}d^{3/2} \tag{7}$$

The energy damping phenomenon in the absorbing boundary follows the relationship below:

$$\kappa_i=\frac{3\kappa_n}{sin3-3}\left\{cosh\left(\frac{3b_i}{W}-1\right)\right\} \tag{8}$$

where κ_i represents a boundary damping function, $b_i\,(i=1,2)$ the horizontal distances in the x and y directions of the absorbing boundary, $\kappa_n=g^{1/2}h^{1/2}$ and W is the width of the absorption boundary.

The energy spectrum used in this simulation was proposed by Bretschneider (1968) with coefficients adjusted by Mitsuyasu (1970) and later Goda(1988, 2000) adjusted the peak frequency and coefficients to give the following expression for the energy spectrum:

$$S(f) = C_1 H_{1/3}^2 \frac{1}{f}\left(T_{1/3} f\right)^{-4} e^{C_2 \left(T_{1/3} f\right)^{-4}} \quad (9)$$

where $S(f)$ is the energy density, $H_{1/3}$ the significant wave height, $T_{1/3}$ the significant wave period and f is the wave frequency that corresponds to the significant wave period. The coefficients C_1 and C_1 are adjusted by many researchers and Goda introduced $C_1 = 0.205$ and $C_2 = -0.75$.

III. Computational Methodology

The above governing equations 1, 2, and 3 have been discretized following a finite difference scheme that uses ADI (Alternating Directional Implicit) algorithm to obtain the solution. In the computational staggered mesh, the x-direction mass flux is defined at the intersection of $(i-1+m)\Delta x$ and $(j-1/2+m)\Delta y$, y-direction mass flux is defined at $(i-1/2+m)\Delta x$ and $(j-1+m)\Delta y$ intersection. On the other hand, instantaneous surface elevation is defined at the junction of $(i-1/2+m)\Delta x$ and $(j-1/2+m)\Delta y$. In all cases $m = 0, 1, 2, \ldots$ In the case of temporal distributions, surface elevations, fluxes in the x- and y-direction are defined at unknown $(n+1/2)\Delta t$, $(n+1)\Delta t$ and $(n+3/2)\Delta t$ time steps. The unknown surface elevations and mass fluxes are computed using their known values until the computation is completed using ADI technique (Hiraishi et al., 1995, Zaman et al., 2001). An energy absorbing boundary shown above by Eq. 8 is employed around the domain to reduce or eliminate the reflected wave components.

IV. Model Validation

The model was validated for limited measured field data obtained from two buoys near the St. John's, Newfoundland coast. This field data was used to validate the applicability of the numerical model in the open sea under normal environmental conditions. The data from the offshore buoy-1 shown in blue in Fig.1 and located at (46.6N, 53.9W) were used as the boundary condition to initialize the numerical model and the predicted results were compared with the measured data at buoy-2 shown in red and located at (46.6N, 53.8W) demonstrated in Fig. 1. The distance between these two buoys was 7.66 km. In the simulation, the predominant wave components and their directions were incorporated in the model boundary condition and any other wave component entering the domain from any other fetch was neglected which is always the case in the open ocean. The computational domain is 2 km wide and 8 km long.

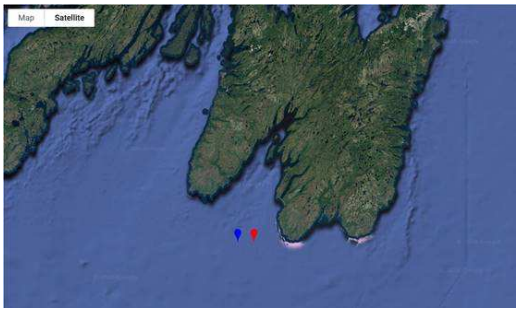

Figure 1 Location of blue dot is 46.6N, 53.9W and red dot is 46.6N, 53.8W (dots are 7.66 km apart)

Table 1 Significant field and numerical data

	Location	$H_{1/3}$(m)	T_p(s)	*h(m)*
Buoy – 1	46.6N, 53.9W	9.823	13.496	53.368
Buoy – 2	46.6N, 53.8W	10.108	13.620	46.413
Present Model	46.6N, 53.8W	9.861	13.584	53.368 to 46.413

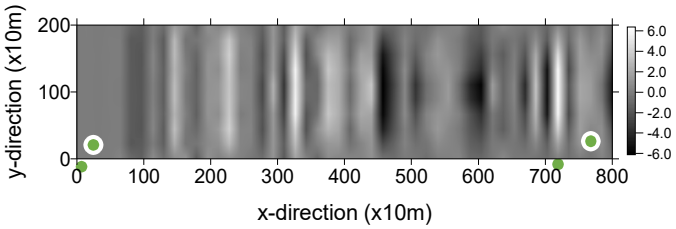

Figure 2 Predicted surface elevations from Buoy-1 to Buoy-2

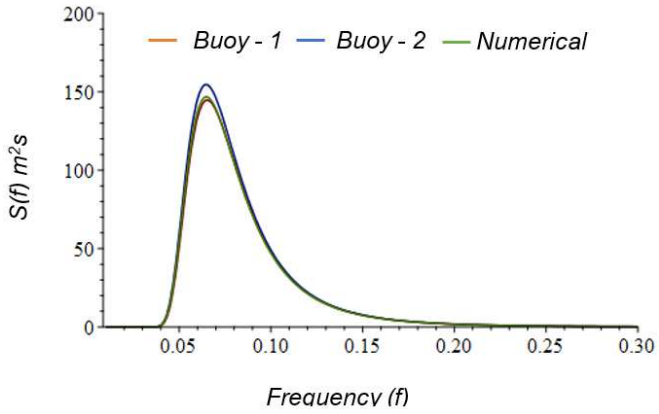

Figure 3 Comparisons of the wave energies at Buoy -1 and Buoy -2 with the present numerical model

Fig. 2 shows the predicted surface elevations on the whole computational domain. The dots on Fig. 2 represent buoy-1 (left) and buoy-2 (right).

Fig. 3 shows the comparison of the measured and simulated results for the power spectrum. The time series of the field data is not available for data storage constraints and only significant wave parameters are available from the field data acquisition authority. So we have used the measured and computed significant wave parameters to generate power spectrum comparisons. It may be observed from Table 1 and Fig. 3 that the measured significant wave heights at buoy-1 and buoy-2 are pretty close and about 2.8% higher at buoy-2 than buoy-1. This is because these buoys are 7.66km apart and many other nomadic wave components may be added and give a rise to the significant wave height at buoy-2. In the numerical model, no extra wave effects were incorporated. But there are substantial unknown parameters that may be responsible for the changes in wave kinematics.

V. Computational Setup

The present model was utilized for different simulations over the bathymetry shown in Fig. 4. The offshore water depth is 45m and the ridge top has a water depth of 10m. The water depth over the flat bottom is 25m over the transmitted zone. The oil rig is situated over the flat bottom having a square shaft of 30m sides that pierced the free surface. A small yellow square represents the rig shaft on the right side of the figures in the results section. The computational domain has a length of 8km and a width of 1.6km for all the computations from now on.

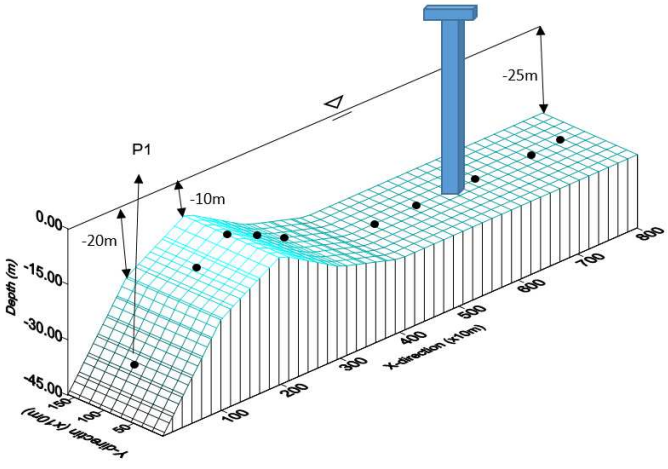

Figure 4 Computational domain with elevated bottom and oil rig

In the simulation, 10 numerical wave probes (Probe-1 to Probe-10) were used. The dots on the ridge were the locations of the numerical probes. A square shaft of 30m sides of the oil rig pierced the free surface. The locations of the wave probes are shown in Table 2.

Table 2 Locations of the wave probes

Probes	*x*-distance (m)	*y*-distance (m)
Probe-1	50	80
Probe-2	150	80
Probe-3	200	80
Probe-4	250	80
Probe-5	300	80
Probe-6	450	80
Probe-7	500	80
Probe-8	625	80
Probe-9	700	80
Probe-10	750	80

VI. Numerical Results and Discussions

The above numerical model is applied to study the propagation and modifications of various waves over the complex bathymetry mentioned above. In the computation, it is assumed that waves approaching from the offshore side towards the ridge. During this process, all waves propagating over this top underwent a lot of changes in their kinematics and profiles. It should be noted that all the wave heights and surface elevations shown here are normalized by the respective significant wave height, the surface elevations used in generating energy computations are prior normalized by the significant wave height. A total of 400 waves are utilized for all irregular wave simulations.

Regular Wave

As test cases, the deformation of a regular wave was studied and shown in this section. In this study, waves with a period of 8s and a height of 4.94m and 9.92m were utilized to introduce a wave steepness of 5.0% and 10.0% as shown in Table 3.

Table 3 Incident regular waves

Cases	*H (m)*	*T (s)*	Steepness (%)
Case-1	4.94	8	5.0
Case-2	9.92	8	10.0

Fig. 5 shows the normalized surface elevations at Probe-1 to Probe-10 for Case-1. In this case, no breaking took place. Part of the wave energies would be reflected from the bottom formation and the rest will propagate over the domain shown in Fig. 4. It can be perceived from Fig. 5 that wave shoaling is taking place at different wave prove locations over the ridge.

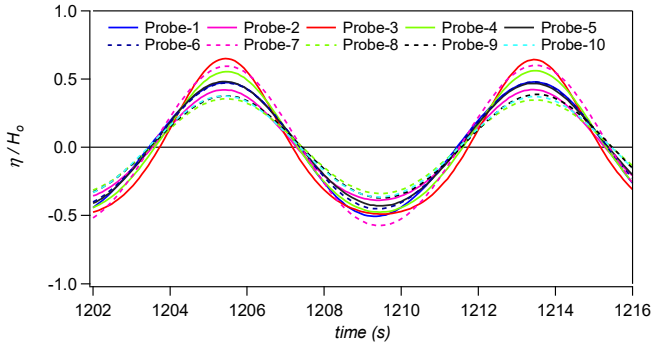

Figure 5 Normalized surface elevations at probes P1 to P10 for Case-1

Fig. 5 also describes that the decrease of the water depths generates considerable nonlinearities in the wave profiles, especially over the ridge and shallow water region. The wave crests turn steeper while the troughs become flatten. The wave propagates with reduced energy and thus the surface elevation decreases over the transmitted area and again part of the wave energies will be reflected from the shaft of the rig.

Fig. 6 shows the horizontal velocity distribution profiles normalized by the wave celerity (C_o = 12.4 m/s) at all 10 wave probe locations.

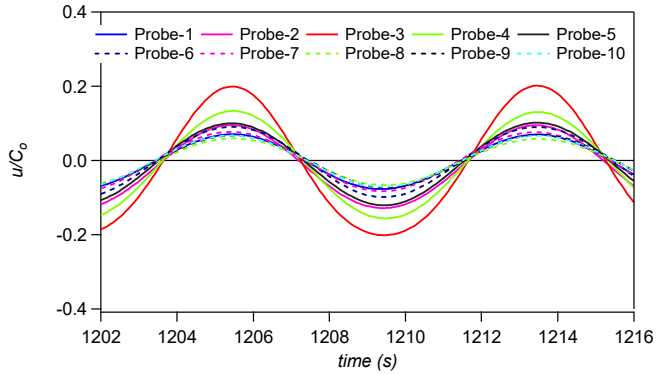

Figure 6 Normalized horizontal velocity profiles at probes P1 to P10 for Case-1

From Fig. 6, it may be observed that the horizontal wave velocity reduces substantially in front of the oil rig (Probe-6 and 7) which implies that the shaft of the oil rig experienced lower hydrodynamic forces.

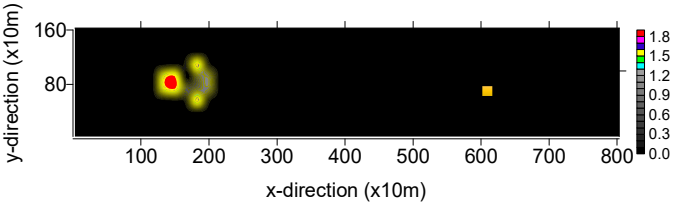

Figure 7 Locations of the wave breaking in the domain for Case-2

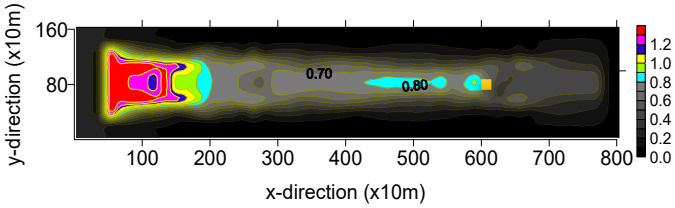

Figure 8 Wave height distribution before and after wave breaking for Case-2

On the other hand, in Case-2 wave reached the breaking criteria, and consequently breaking took place. Fig. 7 shows the wave-breaking locations in the domain. The yellow square in the figures shows the location of the oil rig shaft. The scale with Fig. 7 shows the intensity of the wave breaking where zero (0.0) means no breaking occurs. It is seen in Fig. 8 that after wave breaking the wave heights turn smaller over the transmission region and again get reflected from the shaft of the oil rig.

Irregular Waves

A wave of significant wave period $T_{1/3}$ =12s is utilized for various wave steepness. Table 4 shows the wave parameters for these cases.

Table 4 Irregular waves with varying steepness

Cases	H_s (m)	T_s (s)	Steepness (%)
Case-3	4.94	12	2.5
Case-4	7.99	12	4.0
Case-5	9.99	12	5.0
Case-6	11.98	12	6.0

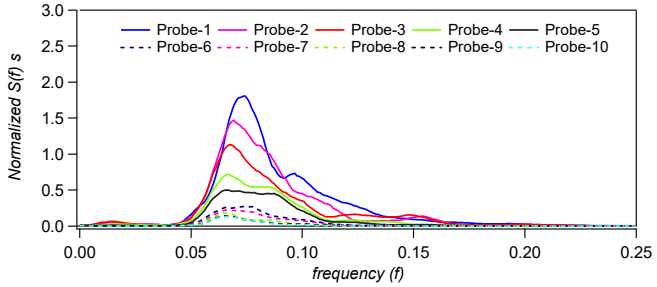

Figure 9 Power spectrum at all 10 probe locations for Case-3

Fig. 9 shows the energy spectrum at all ten probe locations for Case-3. The steepness of the incident wave is 2.5% at the offshore region before the wave entering the computational domain. In all irregular wave simulations, 400 wave components are utilized.

The above figure demonstrates the reduction of the wave energies while the waves propagate from the offshore area to the area of interest that included a complex bathymetry and an oil rig. So the oil rig will experience lesser wave energies due to the wave reflection and loss of energy due to viscous damping.

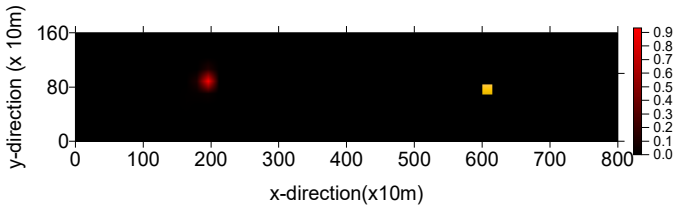

Figure 10a Locations of the wave breaking in the domain for Case-4

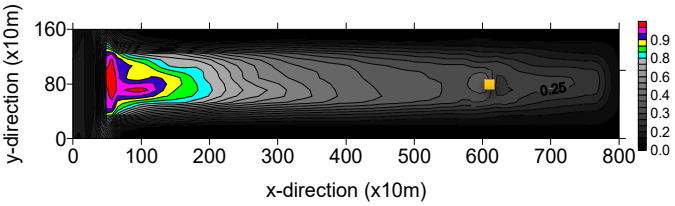

Figure 10b Wave height distribution before and after wave breaking for Case-4

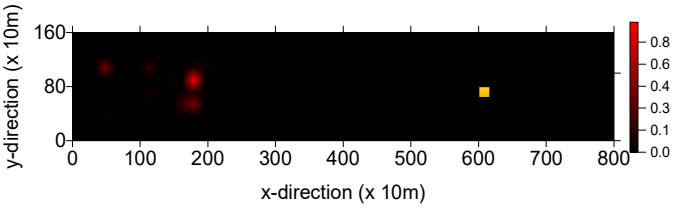

Figure 11a Locations of the wave breaking in the domain for Case-4

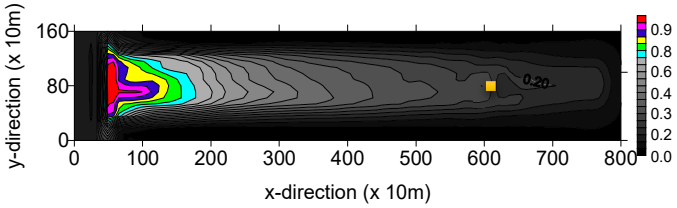

Figure 11b Wave height distribution before and after wave breaking for Case-5

In the numerical simulations, wave breaking take place for Case-4, Case-5, and Case-6 over the elevated bottom of the domain. Fig. 10a-b, 11a-b and12a-b, respectively, show the wave breaking locations on the domain and the distribution of the significant wave heights over the domain for the above three cases. From Figs. 10a, 11a, and 12a, it may be observed that with the increase of the wave steepness wave breaking spread over the wide area in the domain shown by red spots. On the other hand, Figs. 10b, 11b, and 12b show the distribution of the significant wave heights all over the domain. It may be noted

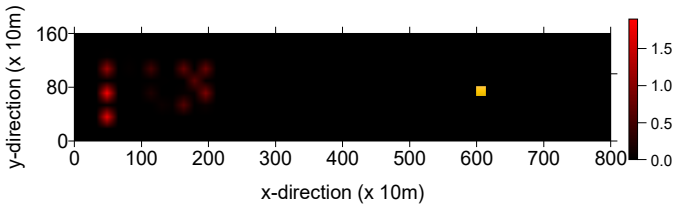

Figure 12a Locations of the wave breaking in the domain for Case-6

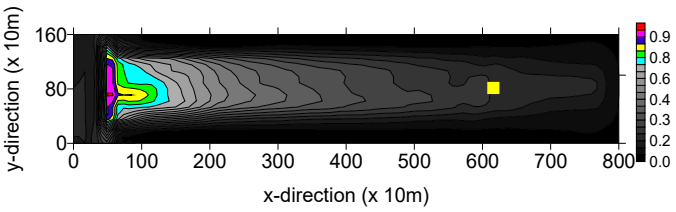

Figure 12b Wave height distribution before and after wave breaking for Case-6

here that the computed significant wave heights are normalized by the incident significant wave height.

Figs. 13 show the comparisons of the energy distributions at

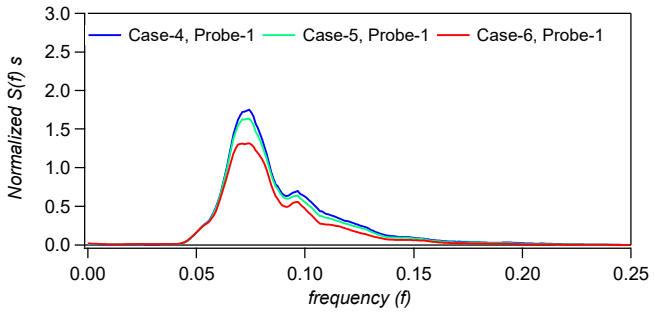

Figure 13a Comparisons of wave energies at Probe-1 for Case-4, Case-5 and Case-6

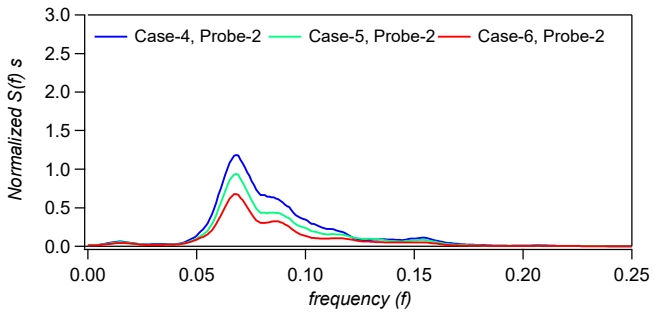

Figure 13b Comparisons of wave energies at Probe-2 for Case-4, Case-5 and Case-6

different probe locations from Probe-1 to Probe-10. Due to the presence of the elevated bottom, there will be considerable wave reflections and also it is shown in Figs. 11, 12 and 13 that with the increase of the wave steepness wave breaking upsurges. After reflection and breaking, the wave reforms and keeps propagating downstream.

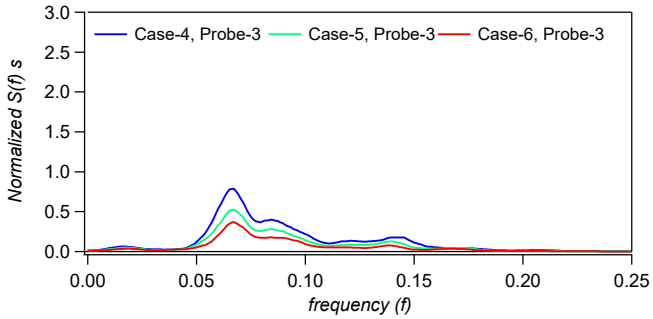

Figure 13c Comparisons of wave energies at Probe-3 for Case-4, Case-5 and Case-6

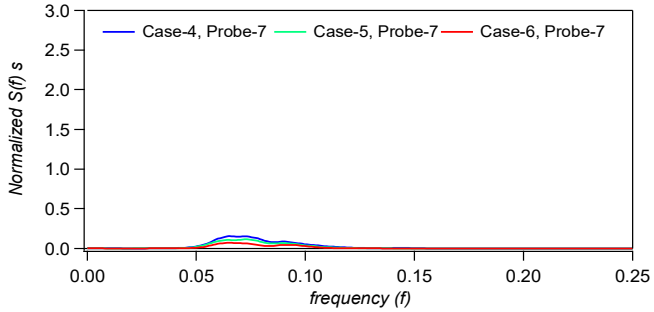

Figure 13g Comparisons of wave energies at Probe-7 for Case-4, Case-5 and Case-6

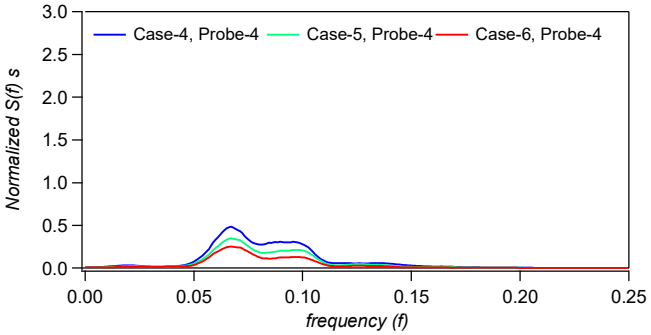

Figure 13d Comparisons of wave energies at Probe-4 for Case-4, Case-5 and Case-6

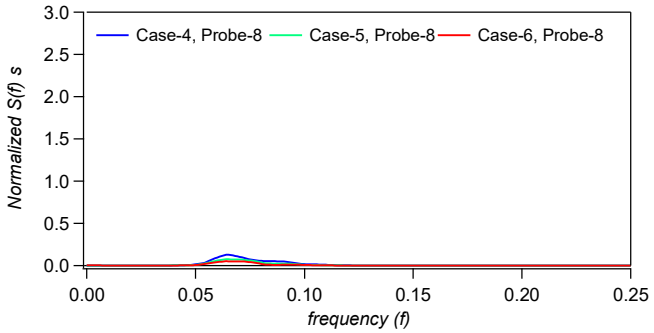

Figure 13h Comparisons of wave energies at Probe-8 for Case-4, Case-5 and Case-6

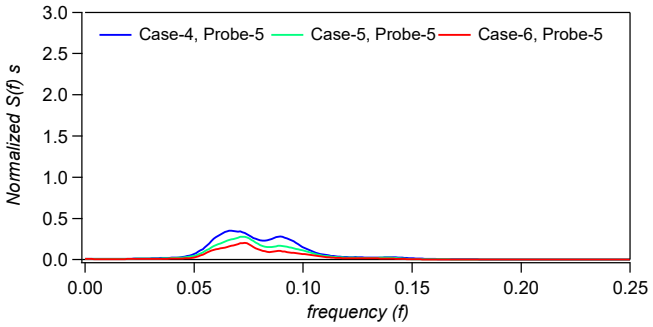

Figure 13e Comparisons of wave energies at Probe-5 for Case-4, Case-5 and Case-6

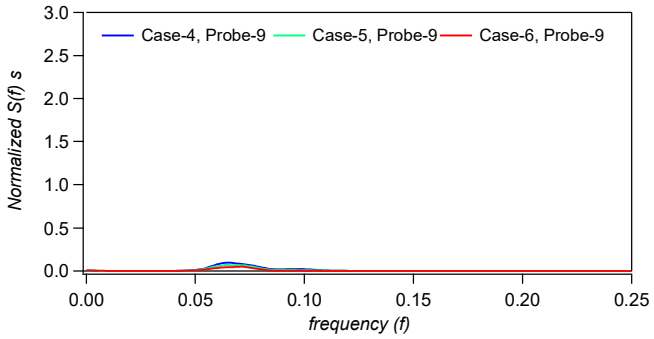

Figure 13i Comparisons of wave energies at Probe-9 for Case-4, Case-5 and Case-6

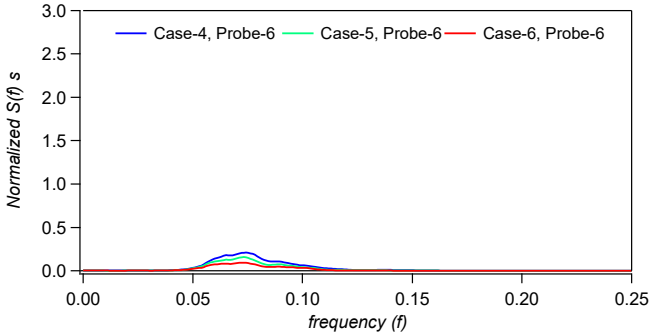

Figure 13f Comparisons of wave energies at Probe-6 for Case-4, Case-5 and Case-6

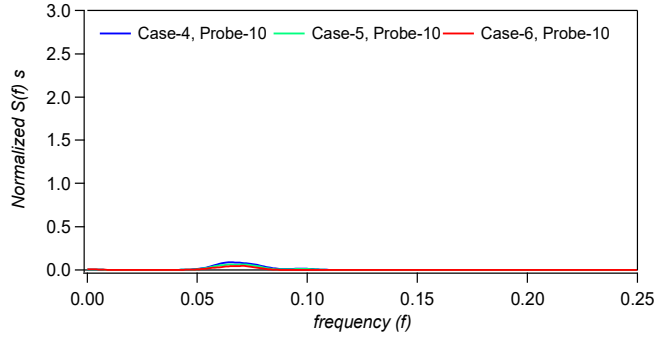

Figure 13j Comparisons of wave energies at Probe-10 for Case-4, Case-5 and Case-6

From all Fig. 13, it is perceived that with the increase of the wave reflections and breaking, the wave energy which is maximum at Probe-1 decreases unceasingly at all other probe locations over the downstream side. The energy for Case-6 is the lowest as the maximum wave breaking occurs for this case.

Loading on the oil rig shaft

Fig. 13g shows the wave energy captured in front of the oil rig shaft by Probe-7 for Case-4, Case-5, and Case-6. Waves with less than 10% energy on average reach the shaft compared to the incident wave energy captured at Prove-1 shown in Fig. 13a. In the Morison equation, the total wave load on the shaft is the summation of the drag force (F_D) and inertia force (F_I) that are proportional to the wave velocity and acceleration components, respectively at the close vicinity of the structure.

$$F = F_D[\propto (u|u|)] + F_I[\propto (\dot{u})] \quad (10)$$

Here F_D is the drag and F_I is the inertia force. The drag and mass coefficients are also important factors that dominate the resulted wave loads. These coefficients are usually evaluated using experimental data or by some empirical method.

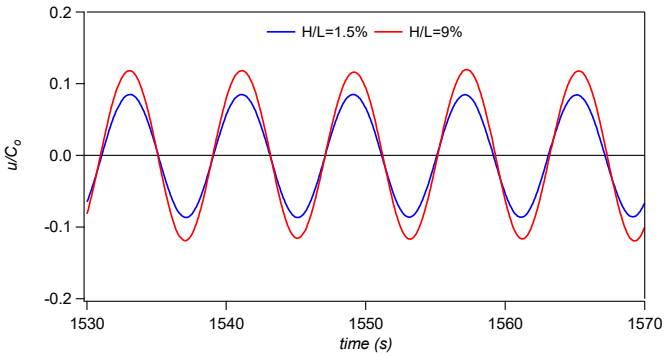

Figure 14 Normalized wave velocities in front of the shaft at Probe-7 for Case-1 and Case-2

Fig. 14 shows the comparisons of the normalized horizontal wave velocity at Probe-7 located in front of the shaft for regular waves mentioned in Case-1 and Case-2.

On the other hand, Fig. 15 shows the time-varying velocity distribution for Case-4, Case-5, and Case-6.

It may be discerned from Fig. 14 and Fig. 15 that with the increase of the wave steepness the wave velocity increases minimally in front of the shaft at Probe-7 as the wave loses its energies. Wave accelerations are not shown here as the drag forces dominate the wave loads.

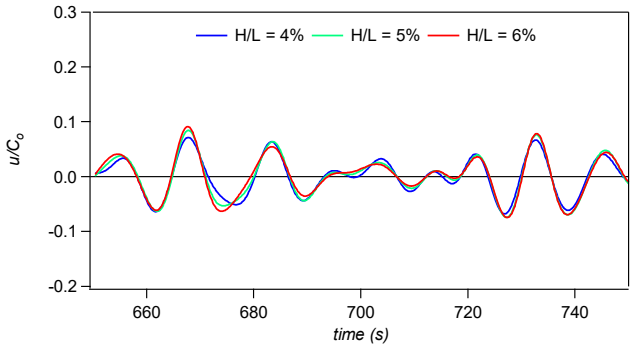

Figure 15 Normalized wave velocities in front of the shaft at Probe-7 for Case-4 Case-5 and Case-6

CONCLUSIONS

A 3D dispersive numerical model with enhanced dispersion characteristics has been formulated and utilized to study the propagation of few cases of regular and irregular waves over an elevated sea bottom. An oil rig is also incorporated in the computational domain to perceive the loadings on it for various breaking and no breaking waves. The proposed model has been utilized to study the propagation, reflection (not shown here), and breaking of the regular and irregular waves over a complex bathymetry in the presence of an oil rig. The model seems identified the locations of the wave-breaking zone and the propagation of the available energy towards the downstream side. It is observed that with the increase of the wave steepness wave breaks, reform and keep propagating and lose energies as they propagate further. The oil rig shaft experiences low energy/loading due to considerable wave reflection from the ridge, wave breaking, and wave attenuation due to viscous effects.

ACKNOWLEDGMENT

All personnel, who have contributed to this project in any form, deserve our sincere gratitude. Funding from NRC-OCRE in the form of the internal project is appreciated.

REFERENCES

[1] Abbott, M. B., H. M. Petersen and O. Skovgaard. “On the numerical modelling of short waves in shallow water.” Journal of Hydraulic Research, 16(3), pp.173-204, 1978.

[2] Bayram, A. and M. Larson. “Wave transformation in the nearshore zone: comparison between a Boussinesq model and field data.” Coastal Engineering, Elsevier, 39, pp.149-171, 2000.

[3] Bretschneider, C. L. “Significant waves and wave spectrum.” Ocean Industries, pp.40-46, 1968.

[4] Flaten, G. and O.B. Rygg. “Dispersive shallow water waves over a porous sea bed.” Coastal Engineering, Elsevier, 15, pp.347-369. 1991.

[5] Goda, Y. “Statistical variability of sea state parameters as a function of a wave spectrum.” Coastal Engineering in Japan 31(1), pp.39-52, 1988.

[6] Goda, Y. “Random seas and design of maritime structures.” World Scientific, pp.1-443, 2000.

[7] Hiraishi, T., I. Uehara and Y. Suzuki. “Applicability of wave transformation model in Boussinesq equations.” Report of the Port and Harbor Research Institute, Japan, No.814, pp.1-22, 1995.

[8] Karambas, TH. V. and C. Koutitas. “A breaking wave propagation model based on Boussinesq equations.” Coastal Engineering, Elsevier, 18, pp.1-19, 1992.

[9] Mitsuyasu, H. “On the growth of spectrum of wind-generated waves (2) - spectral shape of wind waves at finite fetch.” Proc Japanese Conf Coastal Engr, pp.1-7, 1970. In Japanese.

[10] Madsen, P.A. and O.R. Sørensen. “A new form of Boussinesq equations with improved linear dispersion characteristics, Part 2. A slowly varying bathymetry.” Coastal Engineering, Elsevier, 18, pp.183-204, 1992.

[11] Peregrine, G. H. “Long wave on a beach.” JFM, Vol:27, Part:4, pp.715-827, 1967.

[12] Sato, S., M. Kabiling and H. Suzuki. “Prediction of near bottom velocity history by a non-linear dispersive wave model.” Coastal Engineering in Japan 35(1), pp.68-82, 1992.

[13] Sørensen, O.R., P.A. Madsen and H.A. Schäffer, “Nonlinear wave dynamics in the surf zone.” Proc. 25th Coast. Eng. Conf, ASCE, pp.1178-1191, 1996.

[14] Svendsen, I. A., K. Yu and J. Veeramony. “A Boussinesq breaking wave model with vorticity.”, Proc. 25th Coast. Eng. Conf, ASCE, pp.1192-1204, 1996.

[15] Zaman M. H., Hiroyoshi, T. and Baddour, R. E. “Propagation of monochromatic water wave trains.” Ocean Engineering, Elsevier, 34, pp.1850-1862, 2007.

[16] Zaman, M. H, Hirayama, K. and Hiraishi, T. “An extended Boussinesq model and its application to long period waves.” Proc. 11th ISOPE Conf., 3, pp.607-614, 2001.

